Article:
Cao, Y., Ma, S., Zhang, M. et al. (2025) Neuro-Fuzzy Musculoskeletal Model-Driven Assist-as-Needed Control via Impedance Regulation for Rehabilitation Robots. IEEE Transactions on Fuzzy Systems. ISSN: 1063-6706

https://doi.org/10.1109/tfuzz.2025.3611266

Neuro-Fuzzy Musculoskeletal Model-Driven Assist-as-Needed Control via Impedance Regulation for Rehabilitation Robots

Yu Cao, *Member, IEEE*, Shuhao Ma, Mengshi Zhang, Jindong Liu, Jian Huang, *Senior Member, IEEE* and Zhi-Qiang Zhang, *Senior Member, IEEE*

***Abstract*—In rehabilitation applications, encouraging patients to actively participate in training is essential for effective recovery. However, personalized control design in robot-assisted therapy remains challenging due to variations in patients' motor capabilities. To address this issue, this paper proposes an assist-as-needed (AAN) control framework that integrates a hybrid fuzzy-transformer neural network (HFTN) with a fuzzy echo state network (FESN)-based variable impedance controller to ensure personalized support and active engagement. The HFTN integrates fuzzy logic with transformer architectures in parallel paths, combining interpretable modeling of uncertainty in surface electromyography (sEMG) signals with efficient temporal dependency analysis to enhance real-time joint torque estimation. The variable impedance controller constructs the stiffness and damping matrices of the robotic system through the FESN and develops an adaptive update law for the FESN output weights, effectively addressing instability issues in variable stiffness control. Furthermore, driven by physiologically estimated joint torques from the HFTN, the adaption of the FESN reservoir states enables real-time modulation of stiffness and damping, facilitating transitions between human-dominated and robot-dominated modes. This realizes the AAN concept, ensuring personalized and responsive assistance. Various experiments on an upper limb rehabilitation robot were conducted to validate the effectiveness of both the neuro-fuzzy musculoskeletal (MSK) model and the AAN controller in delivering optimal assistance while promoting active user participation.**

***Index Terms*—Assist-as-needed control, hybrid fuzzy-transformer neural network, FESN-based impedance control, impedance regulation.**

I. Introduction

STROKE patients often require long-term rehabilitation due to motor function impairment. Recently, the rehabilitation field has witnessed remarkable advances in robotic therapy [1], [2]. One particularly effective strategy is assist-as-needed (AAN), where the robot offers support only when required [3]. This approach encourages the patient's active participation, ensuring they receive necessary assistance without becoming overly dependent, thereby promoting motor recovery [4]. This means that the key lies in two crucial aspects: accurately assessing the patient's motor abilities and designing appropriate robotic control strategies based on this assessment.

For assessing human motor abilities, common methods in AAN include position/velocity-based [5], [6], force-based [7], position-force hybrid-based [8], [9], and surface electromyography (sEMG)-based approaches [10], [11], [12]. Compared with position/velocity- and force-based methods, the sEMG-based method offers a significant advantage by directly measuring muscle activation signals. This enables a more precise assessment of motor function and allows for earlier and more rapid detection of movement intention, which is particularly beneficial in active rehabilitation training [13]. Nevertheless, relying solely on sEMG is inadequate for accurate joint torque estimation, since joint motor output is also significantly affected by musculoskeletal structure and dynamics. Therefore, integrating musculoskeletal modeling with sEMG analysis holds promise for improving the accuracy of joint torque estimation [14], [15], [16]. However, traditional MSK methods are computationally complex and struggle with personalized modeling, limiting their effectiveness in real-time applications.

Recently, with the advancement of artificial intelligence technology, data-driven approaches have emerged as a viable alternative for MSK modeling, including feed forward neural network (FNN) [17], convolutional neural networks (CNN) [18], recurrent neural networks (RNN) [19], generative adversarial networks (GAN) [20], graph neural networks (GNN) [21], etc. In the recent period, Transformer architectures have garnered significant attention in MSK modeling owing to their sophisticated self-attention mechanisms that efficiently capture temporal dependencies and contextual relationships [22], [23]. Their capability to model complex dynamics and encode long-range dependencies in sequential data renders them particularly advantageous for sEMG feature extraction and representation learning [24], [25]. For instance, Lin et al. [26] developed power- and time-efficient Transformer networks for sEMG-based hand kinematics estimation. Wang et al. [27] developed a dual transformer network (DTN) that simultaneously estimates multiple joint angles and moments

This work was supported in part by the U.K. Research and Innovation (UKRI) Horizon Europe Guarantee under Grant EP/Z001234/1 and Grant EP/Y027930/1, in part by the Royal Society under Grant IEC/NSF/211360, and in part by the National Natural Science Foundation of China under Grant 62333007, and Grant U24A20280. (Yu Cao and Shuhao Ma contributed equally to this work) (Corresponding authors: Jian Huang and Zhiqiang Zhang)

Y. Cao, S. Ma and Z. Zhang are with the School of Electronic & Electrical Engineering, University of Leeds, Leeds, UK (e-mail: y.cao1@leeds.ac.uk, elsma@leeds.ac.uk, z.zhang3@leeds.ac.uk)

J. Huang and M. Zhang are with the Hubei Key Laboratory of Brain-inspired Intelligent Systems, School of Artificial Intelligence and Automation, Huazhong University of Science and Technology, Wuhan, China (e-mail: huang_jan@mail.hust.edu.cn, dream_poem@hust.edu.cn).

J. Liu is with ESTUN Medical Technology Ltd., Nanjing 211106, China (e-mail: liujindong@estun.com).

from multi-channel sEMG signals in the lower limbs. While these methods excel in MSK modeling through automated feature learning and nonlinear mapping, their deterministic architecture struggles with biological uncertainties like noisy sEMG signals and movement variability [28]. This motivates the integration of fuzzy logic principles with neural computation to systematically manage modeling uncertainties, enhance system interpretability via rule-based inference mechanisms, and ensure robustness against measurement noise [29], [30], [31]. Building on this rationale, integrating fuzzy logic with Transformer architectures appears promising for capturing both interpretability and temporal dynamics; however, designing an effective and cohesive fusion framework remains a significant challenge that requires further exploration.

On the other hand, robotic motion control plays a crucial role in implementing AAN. The key is to enable the robot to seamlessly switch between human-dominated and robot-dominated modes, ensuring assistance is provided only when necessary [32]. This requires the robot to regulate its stiffness between low and high levels based on the user's motor ability. Currently, AAN control strategies primarily include position/velocity control based on weighted gains [9], [11], reinforcement learning-based control [33], [34], and variable impedance control [35]. The position/velocity control is heavily dependent on weight adjustments, while reinforcement learning requires large datasets and high computational complexity. In contrast, variable impedance control is especially well-suited for implementing AAN strategies due to its intuitive nature and flexibility for human-robot interaction [36]. But the variation in stiffness may introduce energy into the system, necessitating strict conditions to ensure stability [37]. Neural network-based impedance control methods have shown promise as effective approaches [38]. For instance, Asl et al. [39] proposed a velocity field-based AAN control method utilizing a radial basis function (RBF) neural network. Similarly, Pezeshki et al. [40] incorporated an energy-based performance index into a RBF neural network to realize an AAN strategy. However, these methods primarily interpret impedance variations from an experimental perspective, lacking an explicit and intuitive formulation for the adaption of robotic impedance. This limitation makes it difficult to clearly distinguish between human-dominated and robot-dominated modes. Given the need for both dynamic memory and interpretable structure in adaptive impedance control, the fuzzy echo state network (FESN) offers a promising framework that combines temporal modeling with rule-based logic [41], [42]. Compared to traditional fuzzy logic or fixed mapping methods, which often rely on static rules and lack temporal adaptation, FESN can dynamically evolve stiffness and damping profiles based on input history. This makes it particularly well-suited for modeling time-varying impedance applications. However, employing FESN to construct a variable impedance controller that both ensures system stability and aligns with AAN strategy remains a challenging problem.

To address the aforementioned issues, this paper presents an AAN control framework that integrates a neuro-fuzzy MSK model with a variable impedance controller for active rehabilitation training, ensuring personalized assistance and promoting active user participation. The key contributions of this paper are: 1) We propose a novel data-driven hybrid fuzzy-transformer network (HFTN) for estimating elbow joint torque. This parallel neural architecture seamlessly integrates fuzzy logic with transformer mechanisms, representing the first application of such a hybrid framework in MSK modeling. 2) The joint torques estimated by the HFTN are integrated into the reservoir state adaptation of the FESN-based impedance controller, enabling dynamic modulation of stiffness and damping to achieve a seamless transition between human-dominated and robot-dominated control modes. 3) A series of experimental studies were conducted to validate the data-driven neuro-fuzzy MSK model and the proposed AAN control framework.

The rest of this paper is organized as follows: Section II introduces the dynamics of the rehabilitation robot. Section III presents a HFTN for MSK modeling. Section IV proposes the FESN-based variable impedance control for the AAN strategy. Section V covers experimental studies, and conclusions are drawn in Section VI.

II. Problem Formulation

A. Upper Limb Rehabilitation Robots

The dynamics of a rehabilitation robotic arm with n degrees of freedom (DOF) under human-robot interaction can be described as follows:

$$\boldsymbol{M}(\boldsymbol{q})\ddot{\boldsymbol{q}} + \boldsymbol{C}(\boldsymbol{q},\dot{\boldsymbol{q}})\dot{\boldsymbol{q}} + \boldsymbol{g}(\boldsymbol{q}) = \boldsymbol{\tau} + \boldsymbol{\tau}_e \tag{1}$$

where $\boldsymbol{q} \in \mathbb{R}^n$ is the vector of joint variables, $\boldsymbol{M}(\boldsymbol{q}) \in \mathbb{R}^{n\times n}$ is the inertial matrix, $\boldsymbol{C}(\boldsymbol{q},\dot{\boldsymbol{q}}) \in \mathbb{R}^{n\times n}$ is the centrifugal and Coriolis matrix, $\boldsymbol{g}(\boldsymbol{q}) \in \mathbb{R}^n$ is the vector of gravitational torque. $\boldsymbol{\tau} \in \mathbb{R}^n$ and $\boldsymbol{\tau}_e = \boldsymbol{J}(\boldsymbol{q})^T\boldsymbol{F}_e \in \mathbb{R}^n$ represent the controlled joint torque and human-robot interaction torque applied to the joints because of the external force $\boldsymbol{F}_e \in \mathbb{R}^m$ with the Jacobian $\boldsymbol{J}(\boldsymbol{q}) \in \mathbb{R}^{m\times n}$.

Property 1. *The inertia matrix $\boldsymbol{M}(\boldsymbol{q})$ is symmetric and positive definite, satisfying $\boldsymbol{M}(\boldsymbol{q}) = \boldsymbol{M}(\boldsymbol{q})^T \succ 0$.*

Property 2. *The matrix $\dot{\boldsymbol{M}}(\boldsymbol{q}) - 2\boldsymbol{C}(\boldsymbol{q},\dot{\boldsymbol{q}})$ is skew-symmetric and fulfills the condition:*

$$\boldsymbol{x}_0^T\left(\dot{\boldsymbol{M}}(\boldsymbol{q}) - 2\boldsymbol{C}(\boldsymbol{q},\dot{\boldsymbol{q}})\right)\boldsymbol{x}_0 = 0, \forall \boldsymbol{x}_0 \in \mathbb{R}^n, \tag{2}$$

Property 3. *For $\boldsymbol{A} \in \mathbb{R}^{m\times n}$, $\boldsymbol{B} \in \mathbb{R}^{n\times p}$, $\boldsymbol{C} \in \mathbb{R}^{p\times m}$ and $\boldsymbol{D} \in \mathbb{R}^{m\times n}$, $tr(\cdot)$ operator has the following properties:*

1) $tr(\boldsymbol{A}) = tr(\boldsymbol{A}^T)$;
2) $tr(\boldsymbol{A}+\boldsymbol{D}) = tr(\boldsymbol{A}) + tr(\boldsymbol{D})$;
3) $tr(\boldsymbol{A}^T\boldsymbol{D}) = tr(\boldsymbol{D}^T\boldsymbol{A})$;
4) $tr(\boldsymbol{ABC}) = tr(\boldsymbol{BCA}) = tr(\boldsymbol{CAB})$.

B. Preliminaries

The FESN consists of five layers. The input layer comprises nodes that represent the input variables, denoted as $\boldsymbol{z} = [z_1, ..., z_{N_u}] \in \mathbb{R}^{N_u}$. The second and third layers correspond to the fuzzy logic system (FLS), with the fuzzification layer consisting of N_q neurons and the fuzzy rule layer consisting of N_m neurons, respectively. In the fuzzification

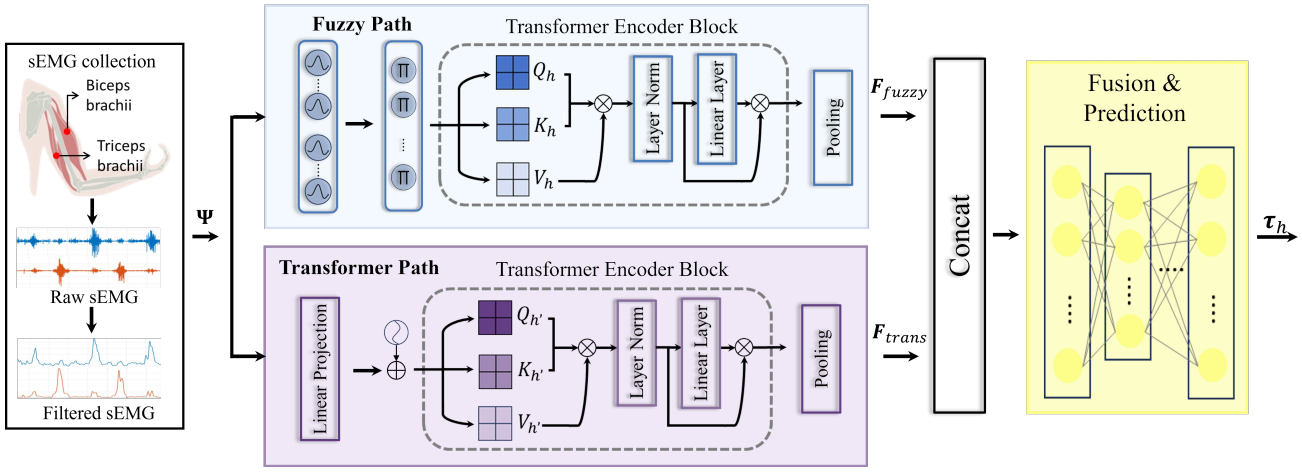

Fig. 1. The framework of HFTN.

layer, the jth membership function for the ith input is modeled a Gaussian functions $\mu_{ij}^k(z_i)$. The output of the fuzzy rule layer is expressed:

$$\Upsilon_k = \prod_{j=1}^{N_q} \mu_{ij}^k, k = 1, ..., N_m \tag{3}$$

Let $\boldsymbol{u}_\Upsilon = [\Upsilon_1, ..., \Upsilon_{N_m}] \in \mathbb{R}^{N_m}$ denote the input to the next layer. Thus, the fourth layer is the dynamic reservoir with internal states $\boldsymbol{\chi} \in \mathbb{R}^N$ governed by the following update law:

$$\dot{\boldsymbol{\chi}} = \tanh(\boldsymbol{W}^i \boldsymbol{u}_\Upsilon + \boldsymbol{W}\boldsymbol{\chi} + \boldsymbol{b}) \tag{4}$$

where $\tanh(\cdot)$ refers to the hyperbolic tangent function. $\boldsymbol{W}^i \in \mathbb{R}^{N\times N_m}$ and $\boldsymbol{W} \in \mathbb{R}^{N\times N}$ represent the input and internal connection weight matrices. $\boldsymbol{b} \in \mathbb{R}^N$ is the bias. The output of the FESN corresponding to the output layer is given by:

$$\boldsymbol{y} = (\boldsymbol{W}^o)^T \boldsymbol{\chi} \tag{5}$$

where $\boldsymbol{y} \in \mathbb{R}^{N_y}$ is the FESN's output. $\boldsymbol{W}^o \in \mathbb{R}^{N\times N_y}$ is the output weight matrix.

III. Neuro-Fuzzy MSK Model

The neuro-fuzzy MSK model is implemented using the proposed HFTN architecture, as illustrated in Fig. 1. The HFTN processes input sEMG signals, $\boldsymbol{\Psi} = \{\boldsymbol{\Psi}_1, \boldsymbol{\Psi}_2\}$, with sequence length S obtained through sliding window segmentation. The signals correspond to the biceps brachii ($\boldsymbol{\Psi}_1$) and triceps brachii ($\boldsymbol{\Psi}_2$) muscles. Each signal is processed through distinct yet complementary pathways to estimate elbow joint torques.

1) Fuzzy Path: The fuzzy path models uncertainty and nonlinearity in sEMG signals through a structured feature extraction approach. Each input dimension connects to a dedicated fuzzy membership layer with M membership functions, computing membership degrees that quantify the relationship between input values and fuzzy concepts, defined as:

$$\mu_{i,j}(\boldsymbol{\Psi}_i) = \exp\left(-\frac{(\boldsymbol{\Psi}_i - c_{i,j})^2}{\sigma_{i,j}^2}\right), j \in \{1, 2, \ldots, M\} \tag{6}$$

where $c_{i,j}$ is the center parameter (fuzzy degree) and $\sigma_{i,j}$ is the width parameter for the j-th membership function of the i-th sEMG channel. The output of the fuzzy membership functions for i-th channel is $\boldsymbol{\mu}_i = [\mu_{i,1}(\boldsymbol{\Psi}_i), \mu_{i,2}(\boldsymbol{\Psi}_i), \ldots, \mu_{i,M}(\boldsymbol{\Psi}_i)] \in \mathbb{R}^{B\times S\times M}$, where B denotes the batch size during the training process. For all membership functions across both channels, the concatenated output is: $\boldsymbol{\mu} = [\boldsymbol{\mu}_1 \parallel \boldsymbol{\mu}_2] \in \mathbb{R}^{B\times S\times 2M}$.

The fuzzy rule layer performs the "AND" fuzzy logic operation between corresponding membership functions [43]:

$$\boldsymbol{R}_j = \mu_{1,j}(\boldsymbol{\Psi}_1) \odot \mu_{2,j}(\boldsymbol{\Psi}_2), \quad j \in \{1, 2, \ldots, M\} \tag{7}$$

where $\odot$ denotes element-wise multiplication. The complete output of the fuzzy rule layer is represented as: $\boldsymbol{R} = [\boldsymbol{R}_1, \boldsymbol{R}_2, \ldots, \boldsymbol{R}_M] \in \mathbb{R}^{B\times S\times M}$.

To enhance the representation power of the fuzzy path, we strategically incorporate a transformer encoder block after the fuzzy rule layer. This transformer block focuses specifically on temporal patterns within the uncertainty-aware fuzzy rule space, enabling effective extraction of temporal relationships between rule outputs across the sequence. For the transformer encoder block, queries $\mathcal{Q}_h$, keys $\mathcal{K}_h$, and values $\mathcal{V}_h$ are derived through linear transformations, the self-attention mechanism is used to model trend dependencies by computing attention scores among every subspace for the target agent:

$$\boldsymbol{A}_h = \text{softmax}\left(\frac{\mathcal{Q}_h(\mathcal{K}_h)^T}{\sqrt{d_k}}\right)\mathcal{V}_h. \tag{8}$$

where $\boldsymbol{A}_h$ denotes the output of each attention head $h \in \{1, 2, \ldots, H\}$. H is the number of heads, and $d_k = M/H$ is the dimension per head. The multi-head attention (MHA) output is: $\text{MHA} = \text{Concat}(\boldsymbol{A}_1, \boldsymbol{A}_2, \ldots, \boldsymbol{A}_H)\boldsymbol{W}_O$, where $\boldsymbol{W}_O$ is a learnable parameter matrix. Following the standard transformer encoder architecture, we implement the first residual connection with layer normalization:

$$\boldsymbol{\Lambda} = \text{LayerNorm}(\boldsymbol{R} + \text{Dropout}(\text{MHA})). \tag{9}$$

Subsequently, $\boldsymbol{\Lambda}$ is processed through a fully connected (FC) network and integrated with the second residual connection:

$$\boldsymbol{F}^{out} = \text{LayerNorm}(\boldsymbol{\Lambda} + \text{Dropout}(\text{FC}(\boldsymbol{\Lambda}))). \tag{10}$$

These dual residual connections effectively mitigate gradient degradation during training. Finally, global average pooling

(GAP) is performed on the transformer encoder output $\boldsymbol{F}^{out}$ to generate the final representation of the fuzzy path:

$$\boldsymbol{F}_{fuzzy} = \frac{1}{S}\sum_{s=1}^{S} \boldsymbol{F}^{out}_{:,s,:} \in \mathbb{R}^{B\times M}. \tag{11}$$

2) Transformer Path: A parallel transformer path directly captures comprehensive sequential dependencies in sEMG signals, extracting pure temporal features that complement the fuzzy path's uncertainty modeling capabilities.

The transformer path comprises several sequential components: Initially, a linear projection layer transforms the input sEMG signals $\boldsymbol{\Psi}$ into a higher-dimensional embedding space:

$$\boldsymbol{F}_{proj} = \mathcal{F}_{\text{proj}}(\boldsymbol{\Psi}) \in \mathbb{R}^{B\times S\times D_{proj}}, \tag{12}$$

where D_{proj} is the embedding dimension of the linear projection layer and $\mathcal{F}_{\text{proj}}(\cdot)$ represents the linear projection operation. Subsequently, a positional encoding layer incorporates information about the absolute positions of tokens within the sequence:

$$\boldsymbol{F}_{pos} = \boldsymbol{F}_{proj} + \mathbf{P} \in \mathbb{R}^{B\times S\times D_{proj}}, \tag{13}$$

where $\mathbf{P}$ represents the positional encoding matrix that integrates sequential position information into the feature representations.

The core architecture of the transformer path consists of $l \in \{1, 2, \ldots, L\}$ transformer encoder blocks implementing MHA mechanisms with H' attention heads, each with dimension $d'_k = D_{proj}/H'$. These transformer encoder blocks share the same architectural configuration as the one in the fuzzy path (identical FC layer, layer normalization operations, and residual connections). The l-th transformer encoder block processes features as follows:

$$\mathbf{F}^{(t,l)} = \mathcal{F}_{\text{Trans}_l}(\mathbf{F}^{(t,l-1)}) \in \mathbb{R}^{B\times S\times D_{proj}}, \tag{14}$$

where $\mathbf{F}^{(t,0)} = \boldsymbol{F}_{pos}$. $\mathcal{F}_{\text{Trans}_l}(\cdot)$ denotes the operation of the l-th transformer encoder block, and $\mathbf{F}^{(t,l)}$ is the resulting output. Following the transformer blocks, GAP is applied, using identical parameters to those employed in the fuzzy logic pathway. This operation yields the final output representation of the transformer pathway $\boldsymbol{F}_{trans}$ as:

$$\boldsymbol{F}_{trans} = \frac{1}{S}\sum_{s=1}^{S} \boldsymbol{F}^{(t,L)}_{:,s,:} \in \mathbb{R}^{B\times D_{proj}}. \tag{15}$$

3) Fusion Part: The fusion part leverages the concept of multi-modal fusion to effectively merge complementary representations from both pathways—interpretable uncertainty-aware features from the fuzzy path ($\boldsymbol{F}_{fuzzy} \in \mathbb{R}^{B\times M}$) and complex temporal dependencies captured by the transformer path ($\boldsymbol{F}_{trans} \in \mathbb{R}^{B\times D_{proj}}$). This process begins with a concatenation operation that combines the $\boldsymbol{F}_{fuzzy}$ and $\boldsymbol{F}_{trans}$ along the feature dimension, creating a unified representation that captures holistic insights:

$$\boldsymbol{F}_{concat} = \text{Concat}(\boldsymbol{F}_{fuzzy}, \boldsymbol{F}_{trans}) \in \mathbb{R}^{B\times(M+D_{proj})}. \tag{16}$$

Then, $\boldsymbol{F}_{concat}$ is transformed through a fusion layer (FC layer followed by ReLU activation function) that projects the combined features into a unified latent space:

$$\boldsymbol{F}_{fused} = \mathcal{F}_{\text{fusion}}(\boldsymbol{F}_{concat}) \in \mathbb{R}^{B\times D_{fusion}}, \tag{17}$$

where $\mathcal{F}_{\text{fusion}}(\cdot)$ represents the fusion operation and D_{fusion} is the dimension of the fused representation space.

The fused representation is lastly processed through a regression component comprising multiple non-linear transformations to generate the final joint torque predictions:

$$\hat{\boldsymbol{\tau}}^n_h = \mathcal{F}_{\text{regression}}(\boldsymbol{F}_{fused}), \tag{18}$$

where $\hat{\boldsymbol{\tau}}^n_h$ represents the predicted joint torques. $\mathcal{F}_{\text{regression}}(\cdot)$ denotes the regression network consisting of three FC layers, each followed by ReLU activation functions except the final output layer, mapping the fused features to the output space. Given the high sampling rate and real-time constraints of our application, this design offers a lightweight and efficient solution for integrating the heterogeneous outputs of the fuzzy and Transformer branches, effectively handling both feature fusion and final regression.

4) Training Strategy: The proposed neural network is trained by minimizing the mean squared error (MSE) between the joint torque values $\hat{\boldsymbol{\tau}}^n_h$ and the ground truth torque values $\boldsymbol{\tau}^n_h$ obtained from OpenSim inverse dynamics. The loss function is formulated as:

$$\mathcal{L}\text{MSE} = \frac{1}{N_s}\sum_{n=1}^{N_s}(\hat{\boldsymbol{\tau}}^n_h - \boldsymbol{\tau}^n_h)^2, \tag{19}$$

where N_s represents the total number of segmented windows.

IV. Controller Design

This controller receives the estimated elbow human joint torque from the neuro-fuzzy MSK model and employs FESN to develop an AAN strategy, operating between human-dominated and robot-dominated modes. Let the desired trajectory $\boldsymbol{q}_d \in \mathbb{R}^n$. The sliding manifold is defined as $\boldsymbol{s}_x = \dot{\boldsymbol{e}} + \boldsymbol{\lambda}_e \boldsymbol{e} \in \mathbb{R}^n$, where $\boldsymbol{\lambda}_e \in \mathbb{R}^{n\times n}$ is a positive definite diagonal matrix, and the tracking error is given by $\boldsymbol{e} = \boldsymbol{q} - \boldsymbol{q}_d \in \mathbb{R}^n$.

To achieve the goal, we first design a novel impedance model with variable stiffness and damping, given by:

$$\begin{aligned}\boldsymbol{\tau}_e = {} & \boldsymbol{M}(\boldsymbol{q})\ddot{\boldsymbol{e}} + (\boldsymbol{D}(t) + \boldsymbol{C}(\boldsymbol{q}, \dot{\boldsymbol{q}}))\dot{\boldsymbol{e}} \\ & + (\boldsymbol{D}(t)\boldsymbol{\lambda}_e + \boldsymbol{C}(\boldsymbol{q}, \dot{\boldsymbol{q}})\boldsymbol{\lambda}_e + \boldsymbol{K}(t) - \boldsymbol{M}(\boldsymbol{q})\boldsymbol{\lambda}_e\boldsymbol{\lambda}_e)\boldsymbol{e}\end{aligned} \tag{20}$$

where $\boldsymbol{D}(t) \in \mathbb{R}^{n\times n}$ and $\boldsymbol{K}(t) \in \mathbb{R}^{n\times n}$ denote the time-varying damping and stiffness, respectively. This removes the requirement for $\boldsymbol{\tau}_e$ sensing by introducing $\boldsymbol{M}(\boldsymbol{q})$ into impedance model, thereby simplifying the implementation of the controller design. Therefore, the control input command is obtain by substituting (20) into (1), given by:

$$\begin{aligned}\boldsymbol{\tau} = {} & \boldsymbol{M}(\boldsymbol{q})\ddot{\boldsymbol{q}}_d + \boldsymbol{C}(\boldsymbol{q}, \dot{\boldsymbol{q}})\dot{\boldsymbol{q}}_d + \boldsymbol{g}(\boldsymbol{q}) - \boldsymbol{D}(t)\boldsymbol{s}_x \\ & - (\boldsymbol{K}(t) + \boldsymbol{C}(\boldsymbol{q}, \dot{\boldsymbol{q}})\boldsymbol{\lambda}_e - \boldsymbol{M}(\boldsymbol{q})\boldsymbol{\lambda}_e\boldsymbol{\lambda}_e)\boldsymbol{e}\end{aligned} \tag{21}$$

Remark 1. *The proposed impedance model (20) departs structurally from the conventional formulation in two key aspects. First, by embedding the robot's inertia and Coriolis*

terms, it eliminates the need for direct human-robot interaction force sensing, enabling sensor-free implementation. Second, by introducing a composite error that couples position and velocity, the model enforces passivity not only in the velocity domain—as in classical designs—but also in the position domain. The dual-channel passivity enhances the overall system stability, facilitates the regulation of velocity and position errors, and strengthens the robustness of human-robot interaction. As a result, the proposed formulation extends the classical impedance model into a more general and practical structure suitable for sensor-limited applications.

A. FESN-based Impedance Generation

Given the complexity of human-robot interaction, we employ an FESN to generate time-varying stiffness $\mathbf{K}(t)$ and damping $\mathbf{D}(t)$ in a dynamic, state-dependent manner, while ensuring closed-loop stability through a Lyapunov-based output weight adaptation law. The output layer is explicitly designed to guarantee passive behaviors of the system, under continuously varying stiffness. The structure of the proposed FESN used for stiffness and damping generation is illustrated in Fig. 2.

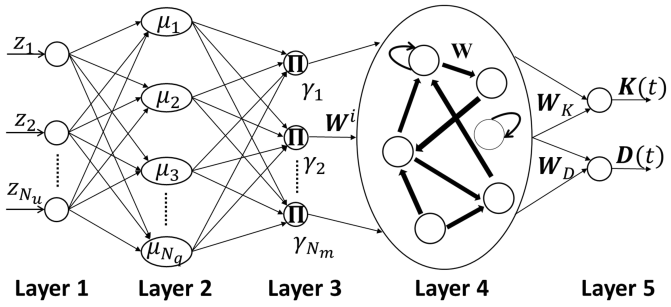

Fig. 2. The framework of the FESN for impedance regulation.

First, we define the FESN output as the robot's stiffness and damping with $\boldsymbol{W}^o = [\boldsymbol{W}_K, \boldsymbol{W}_D] \in \mathbb{R}^{N\times 2n^2}$, given by

$$\left[\boldsymbol{K}_v^T, \boldsymbol{D}_v^T\right]^T = \begin{bmatrix} \boldsymbol{W}_K^T \\ \boldsymbol{W}_D^T \end{bmatrix} \boldsymbol{\chi} \tag{22}$$

where $\boldsymbol{K}_v \in \mathbb{R}^{n^2}$ and $\boldsymbol{D}_v \in \mathbb{R}^{n^2}$ represent the vectorizing the stiffness and damping matrices, denoted as: $\boldsymbol{K}_v = \boldsymbol{W}_K^T\boldsymbol{\chi} = vec(\boldsymbol{K}(t))$ and $\boldsymbol{D}_v = \boldsymbol{W}_D^T\boldsymbol{\chi} = vec(\boldsymbol{D}(t))$ where $vec(\cdot)$ is the column vectorization operator. $\boldsymbol{W}_K \in \mathbb{R}^{N\times n^2}$ and $\boldsymbol{W}_D \in \mathbb{R}^{N\times n^2}$ are the output weight matrices for the FESN.

We propose the adaptive rate of the FESN output layer $\boldsymbol{W}^o$ to counteract the effects of variable stiffness while ensuring that $\boldsymbol{W}^o$ remains ultimately uniformly bounded. The definition of $\dot{\boldsymbol{W}}_K$ and $\dot{\boldsymbol{W}}_D$ are formulated as:

$$\dot{\boldsymbol{W}}_K = \boldsymbol{\varsigma}_K\boldsymbol{\chi}\boldsymbol{\sigma}_K^T - \boldsymbol{\nu}_K\boldsymbol{W}_K \tag{23}$$

$$\dot{\boldsymbol{W}}_D = \boldsymbol{\varsigma}_D\boldsymbol{\chi}\boldsymbol{\sigma}_D^T - \boldsymbol{\nu}_D\boldsymbol{W}_D \tag{24}$$

where $\boldsymbol{\sigma}_K = vec(\boldsymbol{s}_x\boldsymbol{e}^T) \in \mathbb{R}^{n^2}$ and $\boldsymbol{\sigma}_D = vec(\boldsymbol{s}_x\dot{\boldsymbol{e}}^T) \in \mathbb{R}^{n^2}$. $\boldsymbol{\varsigma}_K \in \mathbb{R}^{N\times N}, \boldsymbol{\varsigma}_D \in \mathbb{R}^{N\times N}, \boldsymbol{\nu}_K \in \mathbb{R}^{N\times N}, \boldsymbol{\nu}_D \in \mathbb{R}^{N\times N}$ represent diagonal, positive definite constant matrices.

Theorem 1. *For the robotic system described by (1), with the impedance model given by (20) and the FESN's weight adaptation outlined in (23), the system exhibit the passivity of the dynamics between $\boldsymbol{\tau}_e$ and $\boldsymbol{s}_x$, provided the following condition holds:*

$$\boldsymbol{D}(t) - \boldsymbol{M}(\boldsymbol{q})\boldsymbol{\lambda}_e \succ 0 \tag{25}$$

Proof. A Lyapunov candidate is defined as:

$$V(e) = \frac{1}{2}\boldsymbol{s}_x^T\boldsymbol{M}(\boldsymbol{q})\boldsymbol{s}_x + \frac{1}{2}tr(\boldsymbol{W}_K^T\boldsymbol{\varsigma}_K^{-1}\boldsymbol{W}_K) \tag{26}$$

From Property 2, the derivative of $V(e)$ is:

$$\begin{aligned}\dot{V}(e) &= \boldsymbol{s}_x^T\boldsymbol{M}(\boldsymbol{q})\dot{\boldsymbol{s}}_x + \frac{1}{2}\boldsymbol{s}_x^T\dot{\boldsymbol{M}}(\boldsymbol{q})\boldsymbol{s}_x + tr(\boldsymbol{W}_K^T\boldsymbol{\varsigma}_K^{-1}\dot{\boldsymbol{W}}_K) \\ &= \boldsymbol{s}_x^T(\boldsymbol{M}(\boldsymbol{q})\ddot{\boldsymbol{e}} + \boldsymbol{M}(\boldsymbol{q})\boldsymbol{\lambda}_e\dot{\boldsymbol{e}}) + \frac{1}{2}\boldsymbol{s}_x^T\dot{\boldsymbol{M}}(\boldsymbol{q})\boldsymbol{s}_x \\ &\quad + tr(\boldsymbol{W}_K^T\boldsymbol{\chi}\boldsymbol{\sigma}_K^T - \boldsymbol{W}_K^T\boldsymbol{\varsigma}_K^{-1}\boldsymbol{\nu}_K\boldsymbol{W}_K) \\ &= \boldsymbol{s}_x^T\left(\boldsymbol{\tau}_e - (\boldsymbol{D}(t) - \boldsymbol{M}(\boldsymbol{q})\boldsymbol{\lambda}_e)\,\boldsymbol{s}_x\right) - \boldsymbol{s}_x^T\boldsymbol{K}(t)\boldsymbol{e} \\ &\quad + tr(\boldsymbol{K}_v\boldsymbol{\sigma}_K^T) - tr(\boldsymbol{W}_K^T\boldsymbol{\varsigma}_K^{-1}\boldsymbol{\nu}_K\boldsymbol{W}_K)\end{aligned} \tag{27}$$

According to Property 3, we have

$$\begin{aligned}tr(\boldsymbol{K}_v\boldsymbol{\sigma}_K^T) &= \boldsymbol{\sigma}_K^T\boldsymbol{K}_v = tr\left(\left(\boldsymbol{s}_x\boldsymbol{e}^T\right)^T\boldsymbol{K}(t)\right) \\ &= tr(\boldsymbol{e}\boldsymbol{s}_x^T\boldsymbol{K}(t)) = tr(\boldsymbol{s}_x^T\boldsymbol{K}(t)\boldsymbol{e}) \\ &= \boldsymbol{s}_x^T\boldsymbol{K}(t)\boldsymbol{e}\end{aligned} \tag{28}$$

This implies that the energy generated by the variable stiffness $\boldsymbol{K}(t)$ is offset by the FESN through the output layer adaptation (23). Thus, it follows that

$$\begin{aligned}\dot{V}(e) &= \boldsymbol{s}_x^T\boldsymbol{\tau}_e - \boldsymbol{s}_x^T\left(\boldsymbol{D}(t) - \boldsymbol{M}(\boldsymbol{q})\boldsymbol{\lambda}_e\right)\boldsymbol{s}_x \\ &\quad - tr(\boldsymbol{W}_K^T\boldsymbol{\varsigma}_K^{-1}\boldsymbol{\nu}_K\boldsymbol{W}_K) \\ &= -W + \boldsymbol{s}_x^T\boldsymbol{\tau}_e\end{aligned} \tag{29}$$

where $W = \boldsymbol{s}_x^T(\boldsymbol{D}(t) - \boldsymbol{M}(\boldsymbol{q})\boldsymbol{\lambda}_e)\boldsymbol{s}_x + tr(\boldsymbol{W}_K^T\boldsymbol{\varsigma}_K^{-1}\boldsymbol{\nu}_K\boldsymbol{W}_K) \geq 0$. Thus, we have $W + \dot{V}(e) = \boldsymbol{s}_x^T\boldsymbol{\tau}_e$, the time integral over $[0, t]$ yields

$$\int_0^t \boldsymbol{s}_x^T\boldsymbol{\tau}_e dt = \int_0^t W dt + V(e(t)) - V(e(0)) \tag{30}$$

When $\|\boldsymbol{\tau}_e\|$ is bounded by $\bar{\tau}_e$ ($\|\boldsymbol{\tau}_e\| < \bar{\tau}_e$), we can further obtain:

$$\begin{aligned}\dot{V}(e) &\leq \|\boldsymbol{\tau}_e\|\,\|\boldsymbol{s}_x\| - \lambda_m(\boldsymbol{D}(t) - \boldsymbol{M}(\boldsymbol{q})\boldsymbol{\lambda}_e)\|\boldsymbol{s}_x\|^2 \\ &\leq -\|\boldsymbol{s}_x\|\left(\lambda_m(\boldsymbol{D}(t) - \boldsymbol{M}(\boldsymbol{q})\boldsymbol{\lambda}_e)\,\|\boldsymbol{s}_x\| - \bar{\tau}_e\right)\end{aligned} \tag{31}$$

where $\lambda_m(\cdot)$ denotes the minimum eigenvalue of the matrix. Therefore, $\|\boldsymbol{s}_x\|$ is ultimately uniformly bounded by:

$$\|\boldsymbol{s}_x\| \leq \frac{\bar{\tau}_e}{\lambda_m(\boldsymbol{D}(t) - \boldsymbol{M}(\boldsymbol{q})\boldsymbol{\lambda}_e)} \tag{32}$$

This completes the proof. □

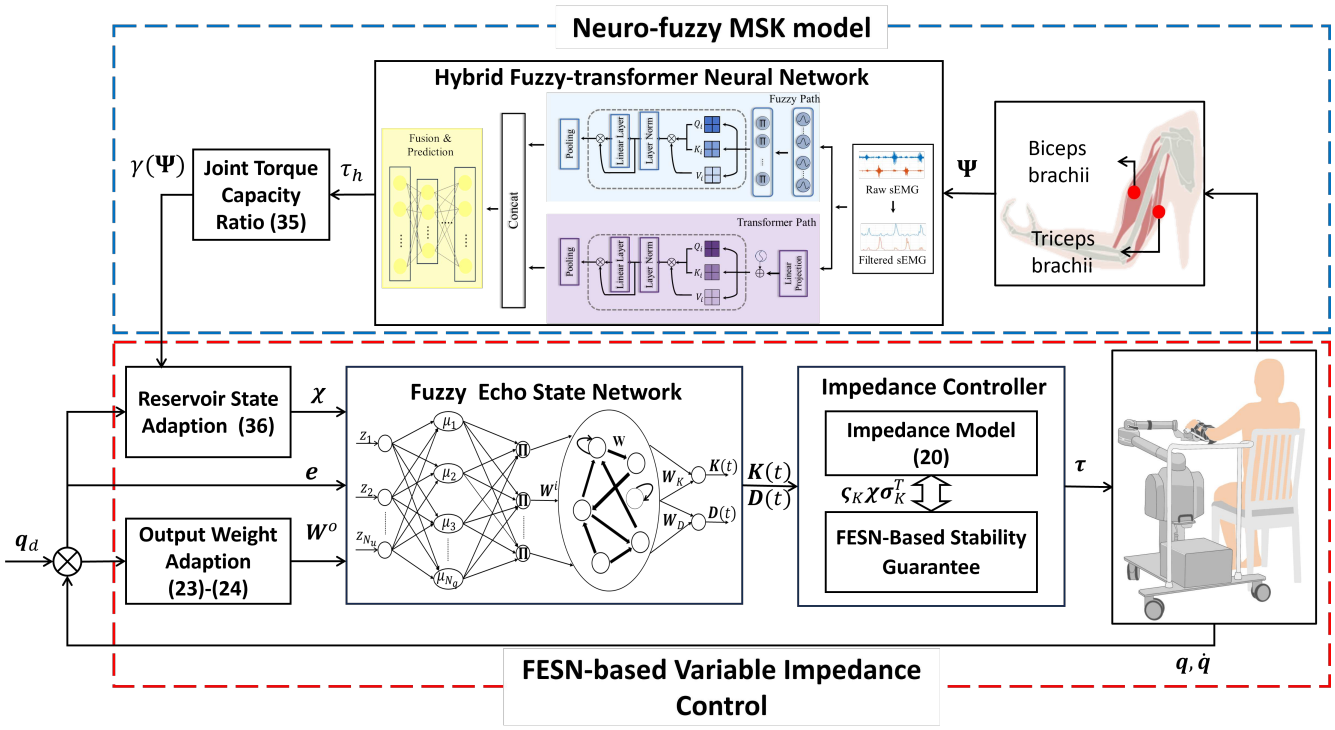

Fig. 3. The framework of the AAN strategy.

B. Impedance Modulation for AAN

Beyond generating stiffness and damping, it is essential in AAN rehabilitation to adapt the system's behavior based on the user's physical effort. To this end, we analyze the variation rates of stiffness $\dot{\boldsymbol{K}}_v$ and damping $\dot{\boldsymbol{D}}_v$ by modulating the internal update rate of the FESN reservoir using the estimated joint torque as an indicator of effort. When user effort is low, the reservoir dynamics are more active, enabling greater stiffness $\mathbf{K}(t)$ and damping $\mathbf{D}(t)$, corresponding to a robot-dominated mode. Conversely, when effort is high, the reservoir activity is suppressed to reduce robotic intervention, forming a human-dominated mode. This effort-aware modulation aligns with the core principles of AAN. The overall control framework is illustrated in Fig. 3.

Substituting (23) and (24) into the derivative of (22) yields:

$$\begin{aligned}\dot{\boldsymbol{K}}_v &= \dot{\boldsymbol{W}}_K^T \boldsymbol{\chi} + \boldsymbol{W}_K^T \dot{\boldsymbol{\chi}} \qquad (33)\\ &= \left(\boldsymbol{\chi}^T \boldsymbol{\varsigma}_K^T \boldsymbol{\chi}\right) \boldsymbol{\sigma}_K - \boldsymbol{\upsilon}_K \boldsymbol{K}_v + \boldsymbol{W}_K^T \dot{\boldsymbol{\chi}}\\ \dot{\boldsymbol{D}}_v &= \dot{\boldsymbol{W}}_D^T \boldsymbol{\chi} + \boldsymbol{W}_D^T \dot{\boldsymbol{\chi}} \qquad (34)\\ &= \left(\boldsymbol{\chi}^T \boldsymbol{\varsigma}_D^T \boldsymbol{\chi}\right) \boldsymbol{\sigma}_D - \boldsymbol{\upsilon}_D \boldsymbol{D}_v + \boldsymbol{W}_D^T \dot{\boldsymbol{\chi}}\end{aligned}$$

From the above formulation, $\dot{\boldsymbol{K}}_v$ and $\dot{\boldsymbol{D}}_v$ are governed by three main components. 1) The term $\left(\boldsymbol{\chi}^T \boldsymbol{\varsigma}_K^T \boldsymbol{\chi}\right) \boldsymbol{\sigma}_K$ and $\left(\boldsymbol{\chi}^T \boldsymbol{\varsigma}_D^T \boldsymbol{\chi}\right) \boldsymbol{\sigma}_D$ represent the gain components, where $\boldsymbol{\chi}^T \boldsymbol{\varsigma}_K^T \boldsymbol{\chi} \in \mathbb{R}^+$ and $\boldsymbol{\chi}^T \boldsymbol{\varsigma}_D^T \boldsymbol{\chi} \in \mathbb{R}^+$ are the positive gain factors. 2) The terms $-\boldsymbol{\upsilon}_K \boldsymbol{K}_v$ and $-\boldsymbol{\upsilon}_D \boldsymbol{D}_v$ account for the decay components for the stiffness and damping. 3) $\boldsymbol{W}_K^T \dot{\boldsymbol{\chi}}$ dictates the regulation pattern for the stiffness and damping. As $\boldsymbol{\chi}^T \boldsymbol{\varsigma}_K^T \boldsymbol{\chi}$ and $\boldsymbol{\chi}^T \boldsymbol{\varsigma}_D^T \boldsymbol{\chi}$ directly influence the rate of variation of the system's stiffness and damping, a well-shaped $\dot{\boldsymbol{\chi}}$ facilitates smooth and adaptive impedance transitions, thereby ensuring stability and effective human-robot interaction.

To enable the estimated human joint torque $\tau_h(\boldsymbol{\Psi})$ from neuro-fuzzy MSK model to directly influence the robot impedance, a joint torque capacity ratio (JTCR) is defined as:

$$\gamma(\boldsymbol{\Psi}) = \frac{1}{1 + \exp(-k_0(\tau_h(\boldsymbol{\Psi}) - \tau_m))} \qquad (35)$$

where τ_m denotes the maximum human joint torque, and k_0 is a slope parameter that controls the rate of transition. Accordingly, $0 < \gamma(\boldsymbol{\Psi}) < 1$ is integrated into the dynamics of $\dot{\boldsymbol{\chi}}$ to regulate the robot's impedance adaptation rate.

The dynamics for $\dot{\boldsymbol{\chi}}$ in (4) is redesigned as:

$$\dot{\boldsymbol{\chi}} = -\gamma(\boldsymbol{\Psi}) \boldsymbol{W} \boldsymbol{\chi} + (1 - \gamma(\boldsymbol{\Psi})) \left(\boldsymbol{W}^i \boldsymbol{u}_\gamma + \boldsymbol{b}\right) \qquad (36)$$

The design includes the following three key aspects:

1) $0 < \gamma(\boldsymbol{\Psi}) < 1$ primarily determines the rate of $\boldsymbol{\chi}$ and thereby influencing the evolution of $\dot{\boldsymbol{K}}_v$ and $\dot{\boldsymbol{D}}_v$. Specifically, as $\gamma(\boldsymbol{\Psi}) \to 0$, the decay rate of $\boldsymbol{\chi}$ decreases, allowing the term $\left(\boldsymbol{W}^i \boldsymbol{u}_\gamma + \boldsymbol{b}\right)$ to exert a greater influence. Consequently, $\|\boldsymbol{\chi}\|$ increases, resulting in larger gain term coefficients $\boldsymbol{\chi}^T \boldsymbol{\varsigma}_K^T \boldsymbol{\chi}$ and $\boldsymbol{\chi}^T \boldsymbol{\varsigma}_D^T \boldsymbol{\chi}$, which enhance system stiffness and damping, and lead to a robot-dominated mode. Conversely, as $\gamma(\boldsymbol{\Psi}) \to 1$, $\boldsymbol{\chi}$ decays rapidly, diminishing the effect of $\left(\boldsymbol{W}^i \boldsymbol{u}_\gamma + \boldsymbol{b}\right)$. This decreases the coefficient $\boldsymbol{\chi}^T \boldsymbol{\varsigma}_K^T \boldsymbol{\chi}$ and $\boldsymbol{\chi}^T \boldsymbol{\varsigma}_D^T \boldsymbol{\chi}$, lowering system stiffness and damping, and promoting a human-dominated mode. The continuous $\gamma(\boldsymbol{\Psi})$ ensures a smooth transition between human-dominated and robot-dominated modes.

2) The internal weight matrix $\boldsymbol{W}$ of the reservoir must be designed to be positive definite to ensure the boundedness of $\boldsymbol{\chi}$, thereby enabling dynamic regulation of the impedance.

3) Let $\boldsymbol{z} = \left[\boldsymbol{e}^T, \dot{\boldsymbol{e}}^T\right]^T$ denote the input to the FESN in (4). According to Theorem 1, $\|\boldsymbol{z}\|$ is ultimately uniformly bounded. The term $\boldsymbol{u}_\Upsilon$ represents the fuzzified state of the FESN, and $\|\boldsymbol{u}_\Upsilon\|$ is also bounded.

Lemma 1. *Let $\boldsymbol{\chi}$ evolve according to the dynamics in (36), with $\gamma(\boldsymbol{\Psi})$ defined by (35). If the input $\boldsymbol{u}_\gamma$ is uniformly bounded such that $\|\boldsymbol{u}_\gamma\| \leq \bar{u}_\gamma$, and the matrix $\boldsymbol{W}$ is positive definite, then the state $\boldsymbol{\chi}$ is ultimately bounded such that*

$$\|\boldsymbol{\chi}(t)\| \leq \bar{\chi}, \quad for \quad \bar{\chi} > 0. \tag{37}$$

Proof. We define a Lyapunov candidate as:

$$V(\chi) = \frac{1}{2}\boldsymbol{\chi}^T\boldsymbol{\chi} \tag{38}$$

Its derivative yields:

$$\begin{aligned}\dot{V}(\chi) &= \frac{1}{2}\boldsymbol{\chi}^T\dot{\boldsymbol{\chi}} \\ &= \boldsymbol{\chi}^T(-\gamma(\boldsymbol{\Psi})\boldsymbol{W}\boldsymbol{\chi} + (1-\gamma(\boldsymbol{\Psi}))\left(\boldsymbol{W}^i\boldsymbol{u}_\gamma + \boldsymbol{b}\right)) \\ &= -\gamma(\boldsymbol{\Psi})\boldsymbol{\chi}^T\boldsymbol{W}\boldsymbol{\chi} + (1-\gamma(\boldsymbol{\Psi}))\,\boldsymbol{\chi}^T(\boldsymbol{W}^i\boldsymbol{u}_\gamma + \boldsymbol{b}) \\ &\leq -\gamma(\boldsymbol{\Psi})\lambda_{\mathrm{m}}(\boldsymbol{W})\|\boldsymbol{\chi}\|^2 \\ &\quad + (1-\gamma(\boldsymbol{\Psi}))\left(\left\|\boldsymbol{W}^i\right\|\bar{u}_\gamma + \|\boldsymbol{b}\|\right)\|\boldsymbol{\chi}\|\end{aligned} \tag{39}$$

Therefore, $\|\boldsymbol{\chi}\|$ is ultimately uniformly bounded by:

$$\|\boldsymbol{\chi}\| \leq \bar{\chi} = \frac{\bar{u}_\gamma\left\|\boldsymbol{W}^i\right\| + \|\boldsymbol{b}\|}{\rho_\gamma\lambda_m(\boldsymbol{W})}, \rho_\gamma = \frac{\gamma(\boldsymbol{\Psi})}{(1-\gamma(\boldsymbol{\Psi}))} \tag{40}$$

This completes the proof. □

Lemma 2. *If $\boldsymbol{W}^o$ evolves according to the adaptive laws given in (23) and (24), and $\boldsymbol{\chi}$ is govern by the dynamics (36), then $\boldsymbol{W}^o$ remains uniformly bounded.*

Proof. A new Lyapunov candidate is defined as:

$$V(W) = \frac{1}{2}tr(\boldsymbol{W}_K^T\boldsymbol{\varsigma}_K^{-1}\boldsymbol{W}_K) + \frac{1}{2}tr(\boldsymbol{W}_D^T\boldsymbol{\varsigma}_D^{-1}\boldsymbol{W}_D) \tag{41}$$

Its derivative is:

$$\begin{aligned}\dot{V}(W) &= tr(\boldsymbol{W}_K^T\boldsymbol{\varsigma}_K^{-1}\dot{\boldsymbol{W}}_K) + tr(\boldsymbol{W}_D^T\boldsymbol{\varsigma}_D^{-1}\dot{\boldsymbol{W}}_D) \\ &= tr(\boldsymbol{W}_K^T\boldsymbol{\chi}\boldsymbol{\sigma}_K^T) + tr(\boldsymbol{W}_D^T\boldsymbol{\chi}\boldsymbol{\sigma}_D^T) \\ &\quad - tr(\boldsymbol{W}_K^T\boldsymbol{\varsigma}_K^{-1}\boldsymbol{\upsilon}_K\boldsymbol{W}_K) - tr(\boldsymbol{W}_D^T\boldsymbol{\varsigma}_D^{-1}\boldsymbol{\upsilon}_D\boldsymbol{W}_D)\end{aligned} \tag{42}$$

Additionally, $\|\boldsymbol{\chi}\|$ is bounded by $\bar{\chi}$ and Theorem 1 establishes that both $\|\boldsymbol{\sigma}_K\|$ and $\|\boldsymbol{\sigma}_D\|$ are bounded. Consequently, $\dot{V}(W)$ satisfies the following relationship:

$$\begin{aligned}\dot{V}(W) &\leq \|\boldsymbol{\chi}\|\|\boldsymbol{\sigma}_K\|\|\boldsymbol{W}_K\| + \|\boldsymbol{\chi}\|\|\boldsymbol{\sigma}_D\|\|\boldsymbol{W}_D\| \\ &\quad - \lambda_m(\boldsymbol{\varsigma}_K^{-1}\boldsymbol{\upsilon}_K)\|\boldsymbol{W}_K\|^2 - \lambda_m(\boldsymbol{\varsigma}_D^{-1}\boldsymbol{\upsilon}_D)\|\boldsymbol{W}_D\|^2 \\ &\leq \bar{\chi}\boldsymbol{\Lambda}^{oT}\boldsymbol{\Theta} - \boldsymbol{\Theta}^T\begin{bmatrix}\lambda_m(\boldsymbol{\varsigma}_K^{-1}\boldsymbol{\upsilon}_K) & 0 \\ 0 & \lambda_m(\boldsymbol{\varsigma}_D^{-1}\boldsymbol{\upsilon}_D)\end{bmatrix}\boldsymbol{\Theta} \\ &\leq \bar{\chi}\|\boldsymbol{\Lambda}^o\|\|\boldsymbol{\Theta}\| - \min(\lambda_m(\boldsymbol{\varsigma}_K^{-1}\boldsymbol{\upsilon}_K), \lambda_m(\boldsymbol{\varsigma}_D^{-1}\boldsymbol{\upsilon}_D))\|\boldsymbol{\Theta}\|^2\end{aligned} \tag{43}$$

where $\lambda_m(\cdot)$ represents the smallest eigenvalue of the matrix. $\boldsymbol{\Lambda}^o = [\|\boldsymbol{\sigma}_K\|, \|\boldsymbol{\sigma}_D\|]^T, \boldsymbol{\Theta} = [\|\boldsymbol{W}_K\|, \|\boldsymbol{W}_D\|]^T$. Therefore, $\boldsymbol{W}^o$ is uniformly bounded by:

$$\|\boldsymbol{W}^o\| \leq \frac{\bar{\chi}\|\boldsymbol{\Lambda}^o\|}{\min(\lambda_m(\boldsymbol{\varsigma}_K^{-1}\boldsymbol{\upsilon}_K), \lambda_m(\boldsymbol{\varsigma}_D^{-1}\boldsymbol{\upsilon}_D))} \tag{44}$$

This completes the proof. □

Remark 2. *The proposed method retains the essential architectural features of a FESN: a recurrent reservoir with internal state $\boldsymbol{\chi}$, an input-driven update mechanism, and a readout layer that outputs stiffness and damping parameters for variable impedance control. Although the output weights are explicitly constructed rather than learned, and the reservoir dynamics are modulated based on user effort, the overall architecture remains consistent with the canonical FESN formulation. Moreover, the design of the reservoir dynamics (36) ensures desirable memory properties: when $\gamma(\boldsymbol{\Psi})$ approaches 1, the reservoir state exhibits exponential decay, and when $\gamma(\boldsymbol{\Psi})$ approaches 0, it becomes input-driven. This guarantees fading memory and ensures that the reservoir state is uniquely determined by recent input history, thereby preserving the echo state property.*

V. Experimental Studies

The experimental validation will be conducted in three stages: 1) evaluation of the neuro-fuzzy MSK model, 2) assessment of the FESN-based variable impedance controller, and 3) integration of both components to validate the personalized AAN strategy. The physical platform is shown in Fig. 4. Three healthy subjects (S1: age 24, gender male, height, 185 cm, weight 77 kg; S2: age 26, gender male, height 174 cm, weight 66 kg; S3: age 29, gender male, height 173 cm, weight 90.3 kg) participated in the experiment. The ethics approval for experiments with healthy subjects was granted by the Engineering and Physical Sciences Faculty Research Ethics Committee of the University of Leeds (LTELEC-001).

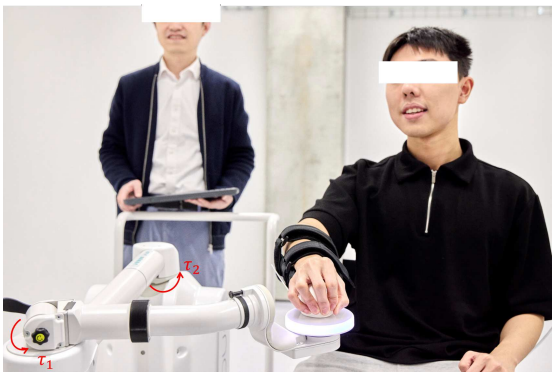

Fig. 4. Rehabilitation robot platform.

A. Neuro-fuzzy MSK Model

The neuro-fuzzy MSK model is tested using sEMG data from biceps and triceps brachii collected via Delsys Trigno™ system at 2148 Hz. Raw signals are preprocessed through second-order Butterworth band-pass filtering (25–450 Hz) for noise removal and fourth-order low-pass filtering (4 Hz) for EMG-force correlation, then normalized using peak isometric maximum voluntary contraction. Filtered sEMG data are prepared for HFTN input using a sliding window with 20-point segments and 2-point stride.

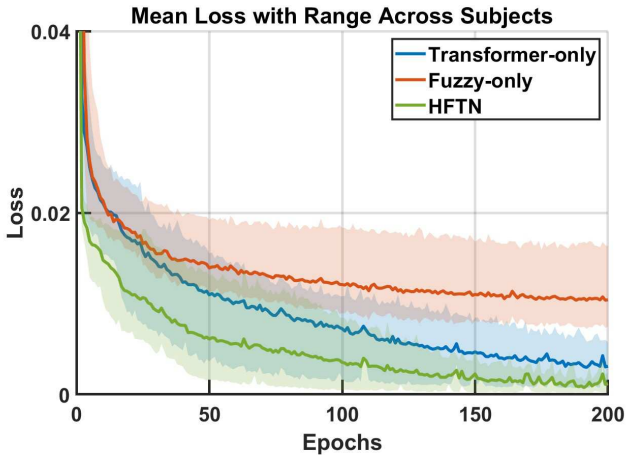

Fig. 5. Comparative analysis of training loss dynamics for three neural network architectures across subjects.

The coefficient of determination R^2 and root mean square error (RMSE) are employed as our primary evaluation metrics. Specifically, the RMSE is defined as:

$$RMSE = \sqrt{\frac{1}{W}\sum_{w=1}^{W}(\boldsymbol{Y}_w - \hat{\boldsymbol{Y}}_w)^2} \tag{45}$$

where W represents the total number of samples in the evaluation dataset after applying the sliding window segmentation, and $\boldsymbol{Y}_w$ and $\hat{\boldsymbol{Y}}_w$ denote the actual values and predicted values at wth sample, respectively. The R^2 value is calculated using the following formula:

$$R^2 = 1 - \frac{\sum_{w=1}^{W}(\boldsymbol{Y}_w - \hat{\boldsymbol{Y}}_w)^2}{\sum_{w=1}^{W}(\boldsymbol{Y}_w - \overline{\boldsymbol{Y}}_w)^2} \tag{46}$$

where $\overline{Y}_w$ indicates the mean value of all the samples in the evaluation dataset.

HFTN is trained using Adam optimizer with learning rate 5×10^{-4}, batch size 16, and up to 200 epochs with early stopping. The transformer components employ embedding dimension $D_{proj} = 32$, $H = H' = 2$ attention heads, $L = 1$ transformer blocks, and FC dimension 32. Dropout rate 0.2 is applied to attention outputs and feed-forward networks. The fuzzy path utilizes $M = 8$ membership functions per input feature. These architectural hyperparameters were selected based on empirical comparisons to balance predictive accuracy and inference efficiency. Regarding the imbalance between the fuzzy and transformer paths, although these two branches differ in both dimensionality (32 vs. 8) and statistical characteristics, we evaluated the impact of this imbalance by introducing L2 normalization prior to feature fusion. This adjustment effectively equalized the magnitude of the two paths, eliminating the dominance of transformer features. However, the performance improvement was marginal (R^2 increase of 0.001; RMSE reduction of 0.002), indicating that the original fusion layer already learned to balance the contributions during training. This suggests that the model is capable of implicitly adjusting the relative influence of each pathway through backpropagation. Therefore, for the sake of architectural simplicity and computational efficiency, we retained the original unnormalized design in the final implementation.

To thoroughly assess each architectural component's contribution, we conducted an ablation study across three subjects evaluating: (a) Transformer-only, (b) Fuzzy-only, and (c) HFTN architectures with consistent parameterization. Fig. 5 presents mean training loss trajectories over 200 epochs, with shaded regions indicating cross-subject variability. The results demonstrate that HFTN exhibits the fastest early convergence (epochs 0-20) and maintains the lowest loss throughout training, ultimately converging to 0.01, compared to Transformer-only (≈ 0.015) and Fuzzy-only (> 0.01). HFTN also displays minimal cross-subject variance, indicating superior generalization capabilities, while Fuzzy-only shows substantial heterogeneity and Transformer-only exhibits moderate variance. These findings support HFTN's superior performance in error minimization, convergence speed, and cross-subject consistency relative to single-paradigm approaches.

Fig. 6 demonstrates HFTN's superior performance compared to Fuzzy-only and Transformer-only architectures. In (a), HFTN attains the highest average R^2 ($\sim$0.97), outperforming Transformer-only ($\sim$0.96) and substantially exceeding Fuzzy-only ($\sim$0.84). In (b), HFTN maintains the lowest RMSE values (0.01-0.03) compared to Transformer-only (0.01-0.04) and Fuzzy-only (0.11-0.12). The minimal variance in HFTN's average RMSE error bars indicates superior stability and generalization. By integrating fuzzy logic with neural networks, HFTN leverages complementary strengths, achieving enhanced predictive accuracy, reduced error rates, and improved cross-subject reliability.

TABLE I
COMPARISON OF MODEL INFERENCE TIME (MS)

Models / Subjects	Transformer-only	Fuzzy-only	HFTN
S1	0.73 ms	0.46 ms	1.05 ms
S2	0.67 ms	0.40 ms	1.03 ms
S3	0.75 ms	0.45 ms	1.02 ms
Average	0.72 ms	0.44 ms	1.03 ms

To quantify real-time performance, we measured inference times on an NVIDIA RTX 3070ti GPU using 500 consecutive operations per model-subject combination with GPU synchronization between iterations. All models achieved inference times below 1.5 ms across subjects (as shown in Table I), well within the 2 ms control cycle required by the robotic system, thereby confirming their suitability for real-time deployment in this application. Also, the proposed HFTN architecture explicitly prioritizes lightweight implementation to meet such real-time constraints. Specifically, the Transformer branch is designed to be compact, comprising only 1 encoder layers, each with 2 attention heads. In parallel, the fuzzy branch operates on a low-dimensional, hand-crafted feature vector, further contributing to the model's simplicity and efficiency. While the HFTN exhibits a slightly longer inference time than the fuzzy-only model, it still maintains a low latency of 1.03 ms-comfortably within the real-time requirement-and delivers superior estimation accuracy.

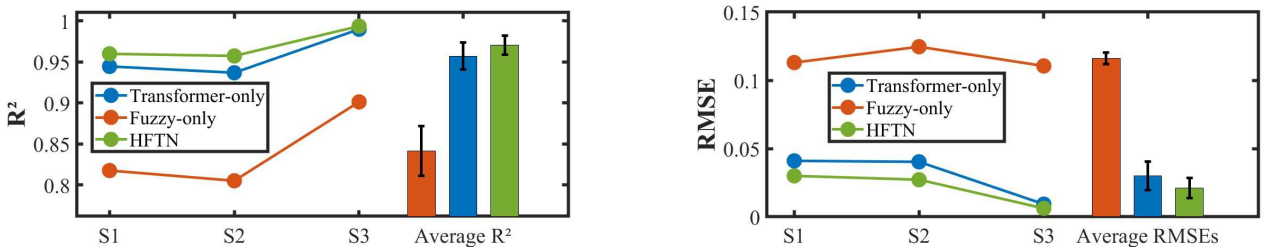

(a) Model Coefficient of Determination Comparison (R^2)

(b) Model Error Comparison (RMSE)

Fig. 6. Performance comparison of three neural network architectures across subjects.

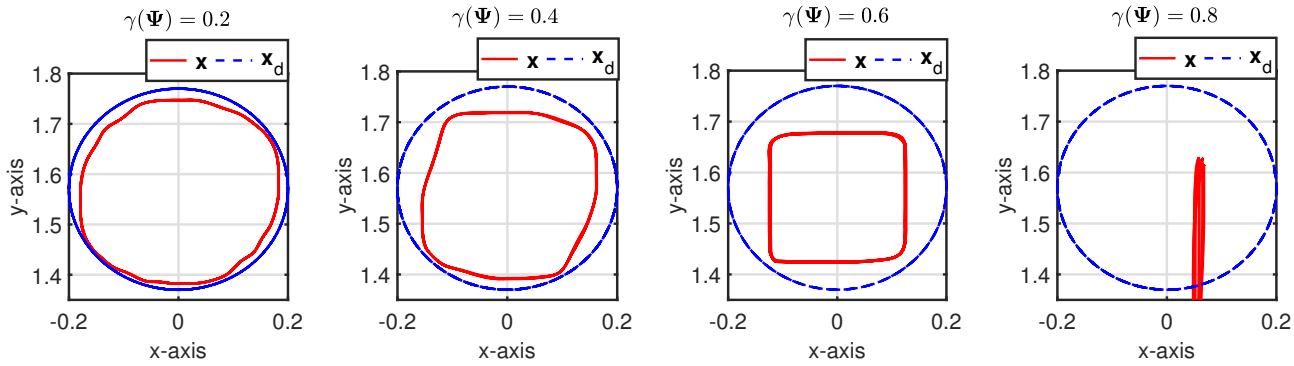

Fig. 7. Tracking performance with specific $\gamma(\Psi) = \{0.2, 0.4, 0.6, 0.8\}$.

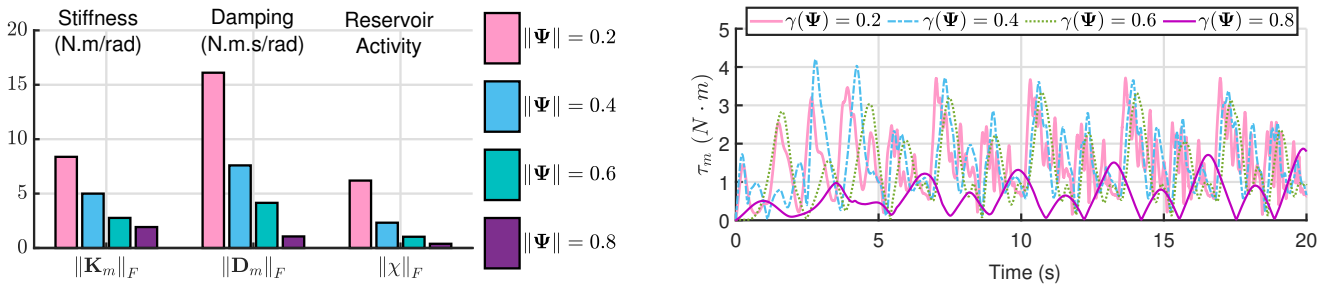

(a) System stiffness, damping, and reservoir activity performance under varying $\gamma(\Psi)$

(b) Motor-generated torque under varying $\gamma(\Psi)$

Fig. 8. Variable impedance controller-related parameters under different $\gamma(\Psi)$.

B. Variable Impedance Controller

The variable impedance controller is implemented on a cable-driven upper-limb rehabilitation robot Burt, developed by ESTUN Medical Technology Co., Ltd. The evaluation focuses on the 2-DOF closest to the end-effector, forming a planar 2-DOF configuration. The robot enables direct joint torque control via a network interface with a 0.002-second sampling interval.

We note that the stiffness and damping values presented in this work are defined at the motor side rather than the joint side of the robot. Due to the presence of gear reduction mechanisms, the actual impedance experienced at the joints is significantly amplified. Let $\mathbf{q}_m = [q_{m1}, q_{m2}]^T$ represent the motor shaft angles, and $\mathbf{q} = [q_1, q_2]^T$ the joint angles. These are related through a linear transformation governed by the gear transmission matrix $\mathbf{R}$, such that:

$$\mathbf{q}_m = \mathbf{R}\,\mathbf{q}, \quad \mathbf{R} = \begin{bmatrix} -15.19 & 0 \\ 0 & -9.57002 \end{bmatrix} \tag{47}$$

Under this transformation, the motor-side torque $\boldsymbol{\tau}_m$ and the joint-side torque $\boldsymbol{\tau}$ are related by the principle of virtual work:

$$\boldsymbol{\tau} = \mathbf{R}^\top \boldsymbol{\tau}_m \tag{48}$$

This relationship indicates that the joint-side torque is amplified proportionally by the gear ratio, consistent with the inverse transformation of angular displacement.

Accordingly, the joint-side stiffness $\mathbf{K}(t)$ and damping $\mathbf{D}(t)$ are computed from the motor-side values $\mathbf{K}_m$ and $\mathbf{D}_m$ via:

$$\mathbf{K}(t) = \mathbf{R}^\top \mathbf{K}_m \mathbf{R}, \quad \mathbf{D}(t) = \mathbf{R}^\top \mathbf{D}_m \mathbf{R} \tag{49}$$

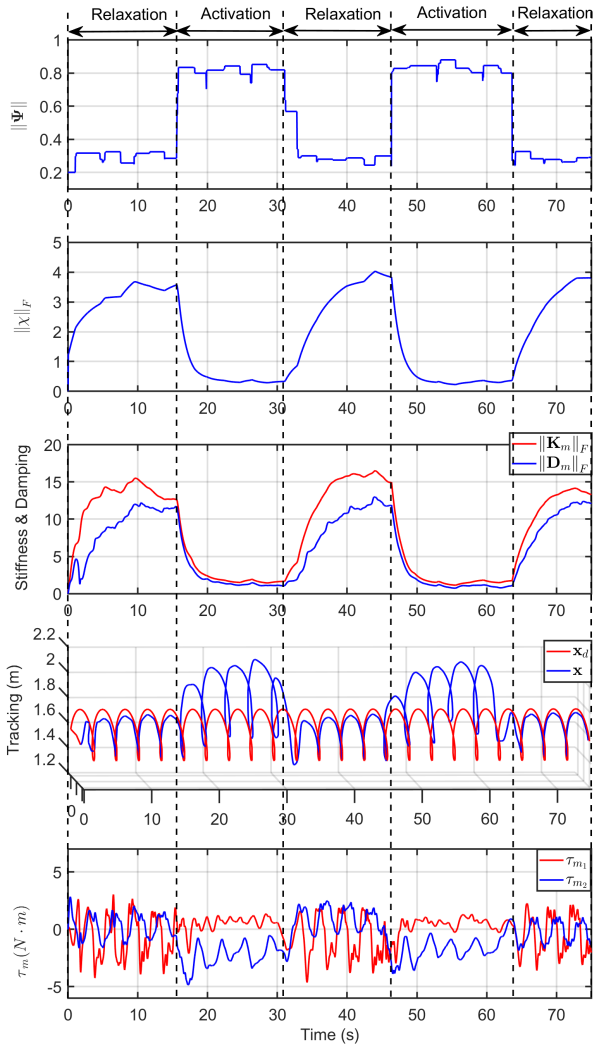

Fig. 9. Time evolution of human-robot interaction under varying human behaviors, including active muscle activation and relaxation states.

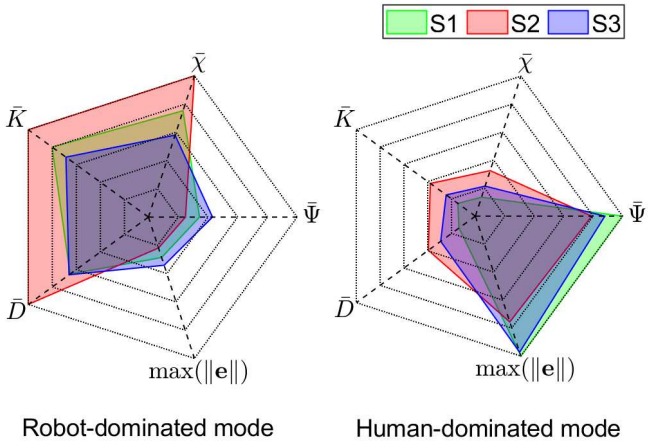

Fig. 10. System behavior during interaction with three individual participants.

This transformation demonstrates that relatively low impedance values at the motor side translate into much higher effective impedance at the joint level.

In this experiment, we set $\gamma(\mathbf{\Psi}) = \{0.2, 0.4, 0.6, 0.8\}$ to evaluate the performance. The results are presented in Fig. 7 and Fig. 8, where the former illustrates the tracking performance, and the latter depicts the controller-related parameters. When $\gamma(\mathbf{\Psi}) = 0.2$, the system achieves relatively high tracking accuracy due to the high reservoir activity, stiffness, and damping, reaching values of $\|\boldsymbol{\chi}\|_F = 6.19$, $\|\boldsymbol{K}_m\|_F = 8.38(N \cdot m/rad)$, and $\|\boldsymbol{D}_m\|_F = 16.11(N \cdot m \cdot s/rad)$. As $\gamma(\mathbf{\Psi})$ increases, the tracking accuracy deteriorates. This is because a larger $\gamma(\mathbf{\Psi})$ leads to a lower steady-state value of $\|\boldsymbol{\chi}\|_F$, which in turn reduces stiffness and damping, as described in (33) and (34). When $\gamma(\mathbf{\Psi})$ increases to 0.8, the value of $\|\boldsymbol{\chi}\|_F$ becomes very small, approaching 0.39. Consequently, the system exhibits significantly low impedance ($\|\boldsymbol{K}_m\|_F = 1.92(N \cdot m/rad)$, $\|\boldsymbol{D}_m\|_F = 1.06(N \cdot m \cdot s/rad)$), making it difficult to track the desired end-effector trajectory $\boldsymbol{x}_d$. Additionally, the input torque further confirms that lower values of $\gamma(\mathbf{\Psi})$ lead to larger input torques and stronger vibrations, increasing sensitivity to tracking errors and, enhancing control accuracy. Therefore, we can conclude that a smaller $\gamma(\mathbf{\Psi})$ increases the system's impedance, enhancing tracking accuracy and placing the robot in a robot-dominated mode. Conversely, a larger $\gamma(\mathbf{\Psi})$ reduces the robot's control effort, allowing the human to easily drive its movement, also resulting in a human-dominated mode.

C. AAN Strategy

In this experiment, we integrate the sEMG acquisition equipment with the rehabilitation robot via a network interface. The calculated JTCR $\gamma(\mathbf{\Psi})$ is transmitted to the robot control board over a network interface at 1058 Hz. As elbow torque rises during flexion and falls during extension, a sliding window is applied to the sEMG to keep robot stiffness low during sustained user effort. Within each window, the maximum value is extracted, as given by:

$$\gamma(\mathbf{\Psi}) = \max\{\gamma(\mathbf{\Psi}(t - \Delta t)), ..., \gamma(\mathbf{\Psi}(t))\} \tag{50}$$

The experimental process is built as follows. Once the system is activated, the human remains passive without exerting any force for 15 seconds. Subsequently, the human begins to apply force to guide the robot's movement, simulating a patient with partial motor function, for another 15 seconds. This is followed by a 15-second period during which the human withdraws the force, representing a scenario where the patient lacks sufficient strength. The human then re-applies force for an additional 15 seconds, and finally, withdraws it again.

The experimental results are shown in Fig. 9. The human joint torque indicator $\gamma(\mathbf{\Psi})$ plays a decisive role in the system's behavior. When $\gamma(\mathbf{\Psi})$ remains at a low level, which indicates that the muscles are inactive and the human is not exerting force (corresponding to 0-15s, 30-45s, and 62-75s), the reservoir activity of the FESN, denoted by $\|\boldsymbol{\chi}\|_F$, gradually increases. This leads to an increase in the output stiffness $\|\boldsymbol{K}_m\|_F$ and damping $\|\boldsymbol{D}_m\|_F$, making the system more responsive to tracking errors. As a result, the control input exhibits stronger vibrations, yielding higher tracking accuracy

and characterizing the robot-dominated mode. In contrast, when $\gamma(\boldsymbol{\Psi})$ reaches a high level, indicating muscle activation around the human elbow joint (corresponding to 15-30s and 45-62s), the reservoir activity of the FESN $\|\boldsymbol{\chi}\|_F$ rapidly decreases. This leads to a reduction in the output stiffness $\|\boldsymbol{K}_m\|_F$ and damping $\|\boldsymbol{D}_m\|_F$. In this state, the system impedance becomes very low, enabling the human to easily guide the robot's motion. Consequently, the system trajectory is less constrained by the desired trajectory and can vary freely, representing the human-dominated mode. Moreover, the transition between the human-dominated mode and the robot-dominated mode is primarily driven by variations in $\gamma(\boldsymbol{\Psi})$, indicating a smooth and continuous shift rather than an abrupt change. This gradual transition contributes to enhanced overall system stability.

Fig. 10 a presents the motion performance metrics of three subjects during both active and passive movement tasks. These metrics include the average human joint effort $\bar{\Psi}$, the robot's average stiffness $\bar{K}$ and damping $\bar{D}$, the average activity level of the FESN reservoir $\bar{\chi}$, and the maximum tracking error $\max(\|\boldsymbol{e}\|)$. A consistent pattern is observed across subjects that aligns well with the earlier theoretical analysis and matches previous experimental results. Individual differences in factors such as muscle strength and the level of active participation lead to subject-specific variations in the robot's performance. Specifically, in the robot-dominated mode, S2 shows lower EMG activity compared to S1 and S3, which results in higher $\bar{\chi}$ and increased $\bar{K}$ and $\bar{D}$. In the human-dominated mode, S1 demonstrates the highest $\bar{\Psi}$, corresponding to the lowest $\bar{K}$ and $\bar{D}$ levels, suggesting that stronger voluntary effort from the human participant effectively directs the robot's motion, resulting in the largest $\max(\|\boldsymbol{e}\|)$.

VI. Conclusion

This paper presents a neuro-fuzzy MSK model-driven variable impedance control framework to implement an AAN strategy for personalized rehabilitation. First, a HFTN is proposed, integrating fuzzy logic with transformer architectures via parallel pathways to enable real-time estimation of human joint torque. Next, a variable impedance controller based on a FESN is developed, incorporating adaptive mechanisms for both the output weight matrices and the internal reservoir states. This enables dynamic switching between human-dominated and robot-dominated interaction modes, thereby achieving the concept of AAN. Extensive experiments confirm that the neuro-fuzzy MSK model and the proposed controller work effectively, showing that the AAN strategy can adapt to users' motor abilities and engagement.

References

[1] M. Kennedy, "The role of collaborative robotics in assistive and rehabilitation applications," *Sci. Robot.*, vol. 8, no. 83, p. eadk6743, 2023.

[2] Y. Cao et al., "Prescribed performance control of a link-type exoskeleton powered by pneumatic muscles with virtual elasticity," Nonlinear Dyn., vol. 112, pp. 10043–10060, 2024.

[3] L. L. Cai, A. J. Fong, Yongqiang Liang, J. Burdick and V. R. Edgerton, "Assist-as-needed training paradigms for robotic rehabilitation of spinal cord injuries," *Proc. IEEE Int. Conf. Robot. Autom. (ICRA)*, 2006. ICRA 2006., Orlando, FL, USA, 2006, pp. 3504-3511

[4] X. Chen, Y. Zheng, Z. Su, Y. Leng, J. Huang and C. Fu, "An Assist-as-Needed Variable Admittance Controller for Adaptive Support of Mobile Walking Assistive Robots," *Proc. 30th Int. Conf. Mechatronics Mach. Vis. Pract. (M2VIP)*, Leeds, United Kingdom, 2024, pp. 1-6

[5] A. Duschau-Wicke, J. von Zitzewitz, A. Caprez, L. Lunenburger and R. Riener, "Path Control: A Method for Patient-Cooperative Robot-Aided Gait Rehabilitation," *IEEE Trans. Neural Syst. Rehabil. Eng.*, vol. 18, no. 1, pp. 38-48, Feb. 2010

[6] R. S. Zarrin, A. Zeiaee and R. Langari, "A Variable-Admittance Assist-As-Needed Controller for Upper-Limb Rehabilitation Exoskeletons," *IEEE Robot. Autom. Lett.*, vol. 9, no. 6, pp. 5903-5910, June 2024.

[7] A. U. Pehlivan, D. P. Losey and M. K. O'Malley, "Minimal Assist-as-Needed Controller for Upper Limb Robotic Rehabilitation," *IEEE Trans. Robot.*, vol. 32, no. 1, pp. 113-124, Feb. 2016

[8] N. Naghavi, A. Akbarzadeh, S. M. Tahamipour-Z., and I. Kardan, "Assist-as-needed control of a hip exoskeleton based on a novel strength index," *Robot. Auton. Syst.*, vol. 134, p. 103667, 2020

[9] Y. Cao, X. Chen, M. Zhang and J. Huang, "Adaptive Position Constrained Assist-as-Needed Control for Rehabilitation Robots," *IEEE Trans. Ind. Electron.*, vol. 71, no. 4, pp. 4059-4068, April 2024.

[10] T. Teramae, T. Noda and J. Morimoto, "EMG-Based Model Predictive Control for Physical Human–Robot Interaction: Application for Assist-As-Needed Control," *IEEE Robot. Autom. Lett.*, vol. 3, no. 1, pp. 210-217, Jan. 2018

[11] N. Garcia-Hernandez, C. Munguia-Angeles and V. Parra-Vega, "Assist-as-Needed Robotic Strategy Based on Velocity Fields for Enhancing Motor Training," *IEEE/ASME Trans. Mechatron.*, doi: 10.1109/TMECH.2024.3445314 (Early access)

[12] C. Xie et al., "A Cable-Driven Upper Limb Rehabilitation Robot With Muscle-Synergy-Based Myoelectric Controller," *IEEE Trans. Robot.*, vol. 40, pp. 3199-3211, 2024

[13] P. Sedighi, X. Li and M. Tavakoli, "EMG-Based Intention Detection Using Deep Learning for Shared Control in Upper-Limb Assistive Exoskeletons," *IEEE Robot. Autom. Lett.*, vol. 9, no. 1, pp. 41-48, Jan. 2024

[14] Y. Dai, J. Wu, Y. Fan, J. Wang, J. Niu, F. Gu, and S. Shen, "MSEva: A musculoskeletal rehabilitation evaluation system based on EMG signals," *ACM Trans. Sens. Networks*, vol. 19, no. 1, pp. 1-23, Feb. 2023

[15] Y. Zhao et al., "An EMG-Driven Musculoskeletal Model for Estimating Continuous Wrist Motion," *IEEE Trans. Neural Syst. Rehabil. Eng.*, vol. 28, no. 12, pp. 3113-3120, Dec. 2020

[16] Y. Cao et al., "Musculoskeletal Model-Based Adaptive Variable Impedance Control With Flexible Prescribed Performance for Rehabilitation Robots," *IEEE/ASME Trans. Mechatron.*, doi: 10.1109/TMECH.2025.3562670. (Early access)

[17] S. Ma et al., "Physics-Informed Deep Learning for Muscle Force Prediction With Unlabeled sEMG Signals," *IEEE Trans. Neural Syst. Rehabil. Eng.*, vol. 32, pp. 1246-1256, 2024

[18] J. Zhang et al., "Physics-Informed Deep Learning for Musculoskeletal Modeling: Predicting Muscle Forces and Joint Kinematics From Surface EMG," *IEEE Trans. Neural Syst. Rehabil. Eng.*, vol. 31, pp. 484-493, 2023

[19] Y. Huang et al., "Real-Time Intended Knee Joint Motion Prediction by Deep-Recurrent Neural Networks," *IEEE Sens. J.*, vol. 19, no. 23, pp. 11503-11509, 2019

[20] Y. Shi, S. Ma, Y. Zhao, C. Shi and Z. Zhang, "A Physics-Informed Low-Shot Adversarial Learning for sEMG-Based Estimation of Muscle Force and Joint Kinematics," *IEEE J. Biomed. Health Informat.*, vol. 28, no. 3, pp. 1309-1320, 2024

[21] A. Vijayvargiya, R. Kumar and P. Sharma, "PC-GNN: Pearson Correlation-Based Graph Neural Network for Recognition of Human Lower Limb Activity Using sEMG Signal," *IEEE Trans. Hum.-Mach. Syst.*, vol. 53, no. 6, pp. 945-954, 2023

[22] Z. Chen, H. Wang, H. Chen, and T. Wei, "Continuous motion finger joint angle estimation utilizing hybrid sEMG-FMG modality driven transformer-based deep learning model," *Biomed. Signal Process. Control*, vol. 85, pp. 105030, 2023

[23] T. Liang et al., "sEMG-Based End-to-End Continues Prediction of Human Knee Joint Angles Using the Tightly Coupled Convolutional Transformer Model," *IEEE J. Biomed. Health Informat.*, vol. 27, no. 11, pp. 5272-5280, 2023

[24] Y. Liu, X. Li, L. Yang and H. Yu, "A Transformer-Based Gesture Prediction Model via sEMG Sensor for Human–Robot Interaction," *IEEE Trans. Instrum. Meas.*, vol. 73, pp. 1-15, 2024

[25] S. A. Zendehbad, A. S. Razavi, M. A. Sanjani, Z. Sedaghat, and S. Lashkari, "TraxVBF: A hybrid transformer-xLSTM framework for EMG signal processing and assistive technology development in rehabilitation," *Sensing Bio-Sens. Res.*, vol. 47, p. 100749, Feb. 2025

[26] C. Lin et al., "Continuous Estimation of Hand Kinematics From Electromyographic Signals Based on Power-and Time-Efficient Transformer Deep Learning Network," *IEEE Trans. Neural Syst. Rehabil. Eng.*, vol. 33, pp. 58-67, 2025

[27] Z. Wang, C. Chen, H. Chen, Y. Zhou, X. Wang and X. Wu, "Dual Transformer Network for Predicting Joint Angles and Torques From Multi-Channel EMG Signals in the Lower Limbs," *IEEE J. Biomed. Health Informat.*, doi: 10.1109/JBHI.2025.3555255

[28] W. Zhong, X. Fu and M. Zhang, "A Muscle Synergy-Driven ANFIS Approach to Predict Continuous Knee Joint Movement," *IEEE Trans. Fuzzy Syst.*, vol. 30, no. 6, pp. 1553-1563, June 2022

[29] J. Lu, G. Ma and G. Zhang, "Fuzzy Machine Learning: A Comprehensive Framework and Systematic Review," *IEEE Trans. Fuzzy Syst.*, vol. 32, no. 7, pp. 3861-3878, July 2024

[30] H. Xia, M. Pi, L. Jin, R. Song and Z. Li, "Human Collaborative Control of Lower-Limb Prosthesis Based on Game Theory and Fuzzy Approximation," *IEEE Transactions on Cybernetics*, vol. 55, no. 1, pp. 247-258, Jan. 2025

[31] C. Chen, Y. Cao, X. Chen, D. Wu, C. Xiong and J. Huang, "A Fused Deep Fuzzy Neural Network Controller and Its Application to Pneumatic Flexible Joint," *IEEE/ASME Trans. Mechatron.*, vol. 28, no. 6, pp. 3214-3225, Dec. 2023

[32] E. T. Wolbrecht, V. Chan, D. J. Reinkensmeyer and J. E. Bobrow, "Optimizing Compliant, Model-Based Robotic Assistance to Promote Neurorehabilitation," *IEEE Trans. Neural Syst. Rehabil. Eng.*, vol. 16, no. 3, pp. 286-297, June 2008

[33] Y. Zhang, S. Li, K. J. Nolan and D. Zanotto, "Adaptive Assist-as-needed Control Based on Actor-Critic Reinforcement Learning," *Proc. IEEE/RSJ Int. Conf. Intell. Robots Syst. (IROS)*, Macau, China, 2019, pp. 4066-4071.

[34] S. Pareek, H. J. Nisar and T. Kesavadas, "AR3n: A Reinforcement Learning-Based Assist-as-Needed Controller for Robotic Rehabilitation," *IEEE Robot. Autom. Mag.*, vol. 31, no. 3, pp. 74-82, Sept. 2024

[35] P. Agarwal and A. D. Deshpande, "Subject-Specific Assist-as-Needed Controllers for a Hand Exoskeleton for Rehabilitation," *IEEE Robot. Autom. Lett.*, vol. 3, no. 1, pp. 508-515, Jan. 2018

[36] Y. Cao, M. Zhang, J. Huang and S. Mohammed, "Load-Transfer Suspended Backpack With Bioinspired Vibration Isolation for Shoulder Pressure Reduction Across Diverse Terrains," *IEEE Trans. Robot.*, vol. 41, pp. 3059-3077, 2025

[37] K. Kronander and A. Billard, "Stability Considerations for Variable Impedance Control," *IEEE Trans. Robot.*, vol. 32, no. 5, pp. 1298-1305, Oct. 2016

[38] G. Li, J. Yu and X. Chen, "Adaptive Fuzzy Neural Network Command Filtered Impedance Control of Constrained Robotic Manipulators With Disturbance Observer," *IEEE Trans. Neural Netw. Learn. Syst.*, vol. 34, no. 8, pp. 5171-5180, Aug. 2023

[39] H. J. Asl, et al., "Field-Based Assist-as-Needed Control Schemes for Rehabilitation Robots," *IEEE/ASME Trans. Mechatron.*, vol. 25, no. 4, pp. 2100-2111, Aug. 2020.

[40] L. Pezeshki, H. Sadeghian, A. Mohebbi, M. Keshmiri and S. Haddadin, "Personalized Assistance in Robotic Rehabilitation: Real-Time Adaptation via Energy-Based Performance Monitoring," *IEEE Trans. Autom. Sci. Eng.*, vol. 22, pp. 13298-13309, 2025

[41] S. I. Han and J. M. Lee, "Fuzzy Echo State Neural Networks and Funnel Dynamic Surface Control for Prescribed Performance of a Nonlinear Dynamic System," *IEEE Trans. Ind. Electron.*, vol. 61, no. 2, pp. 1099-1112, Feb. 2014

[42] Q. Wang, Y. Pan, J. Cao and H. Liu, "Adaptive Fuzzy Echo State Network Control of Fractional-Order Large-Scale Nonlinear Systems With Time-Varying Deferred Constraints," *IEEE Trans. Fuzzy Syst.*, vol. 32, no. 2, pp. 634-648, Feb. 2024

[43] Y. Deng, Z. Ren, Y. Kong, F. Bao and Q. Dai, "A Hierarchical Fused Fuzzy Deep Neural Network for Data Classification," *IEEE Trans. Fuzzy Syst.*, vol. 25, no. 4, pp. 1006-1012, Aug. 2017